Operational modal analysis on a VAWT in a large wind tunnel using stereo vision technique

Najafi, Nadia; Schmidt Paulsen, Uwe

Published in:
Energy

Link to article, DOI:
10.1016/j.energy.2017.02.133

Publication date:
2017

Document Version
Publisher's PDF, also known as Version of record

Energy 125 (2017) 405–416

Contents lists available at ScienceDirect

Energy

journal homepage: www.elsevier.com/locate/energy

Operational modal analysis on a VAWT in a large wind tunnel using stereo vision technique

Nadia Najafi*, Uwe Schmidt Paulsen

Technical University of Denmark, Department of Wind Energy, Denmark

ARTICLE INFO

Article history:
Received 22 August 2016
Received in revised form
19 January 2017
Accepted 22 February 2017
Available online 23 February 2017

Keywords:
Stereo vision
Operational modal analysis
Data-driven SSI
Vertical axis wind turbine
HAWC2
Wind energy

ABSTRACT

This paper is about development and use of a research based stereo vision system for vibration and operational modal analysis on a parked, 1-kW, 3-bladed vertical axis wind turbine (VAWT), tested in a wind tunnel at high wind. Vibrations were explored experimentally by tracking small deflections of the markers on the structure with two cameras, and also numerically, to study structural vibrations in an overall objective to investigate challenges and to prove the capability of using stereo vision. Two high speed cameras provided displacement measurements at no wind speed interference. The displacement time series were obtained using a robust image processing algorithm and analyzed with data-driven stochastic subspace identification (DD-SSI) method. In addition of exploring structural behaviour, the VAWT testing gave us the possibility to study aerodynamic effects at Reynolds number of approximately 2×10^5. VAWT dynamics were simulated using HAWC2. The stereo vision results and HAWC2 simulations agree within 4% except for mode 3 and 4. The high aerodynamic damping of one of the blades, in flatwise motion, would explain the gap between those two modes from simulation and stereo vision. A set of conventional sensors, such as accelerometers and strain gauges, are also measuring rotor vibration during the experiment. The spectral analysis of the output signals of the conventional sensors agrees the stereo vision results within 4% except for mode 4 which is due to the inaccuracy of spectral analysis in picking very closely spaced modes. Finally, the uncertainty of the 3D displacement measurement was evaluated by applying a generalized method based on the law of error propagation, for a linear camera model of the stereo vision system.

1. Introduction

The increasing global demand for electrical power attracts development of efficient renewable energy systems, in particular wind turbines. High COE of wind energy has fostered new ideas in developing genuine designs for offshore wind energy, such as the DeepWind concept [1]. This concept could demonstrate significant COE reductions because of promising potentials in upscaling, simple design, installation and O&M. Despite the simplicity of the VAWT design, the structural response is complex to simulate, and validation requires detailed experiments. In addition, structural response testing conducted with standard loads and vibration sensing equipment would require costly considerations. Traditional transducers such as strain gauges and accelerometers have been used for displacement measurements [2], but they are challenged on the following limitations and drawbacks: i) the implementation usually needs a lot of wiring and interfacing preparations, which is costly and time consuming on large wind turbines [3] ii) accelerometer signals need two levels of integration to get displacement information; this introduces errors due to initial conditions and other computation issues [4]. iii) The sensors might be biased by drift, and they load the structure with their weight and can measure in only a few numbers of points [5]. Even methods involving roving accelerometers over a full-scale wind turbine blade seem to be very time consuming. In addition, in rotating structures like wind turbines, the measured signal from conventional sensors like accelerometers will not be very accurate at low frequencies and is including the centrifugal acceleration.

By applying simple black dots on reflecting or non-reflecting paper they can turn into 3-D sensors, which combined with the stereo vision method enable 3-D displacements measurements. Stereo vision is the 3D reconstruction of an object via two or more 2D images. It takes few preparations and needs little mounting

* Corresponding author.
E-mail addresses: nadn@dtu.dk (N. Najafi), uwpa@dtu.dk (U.S. Paulsen).

http://dx.doi.org/10.1016/j.energy.2017.02.133

List of symbols

$Y_{0\|2i}$	Block Hankel matrix
A	State matrix
B	Input matrix
C	Observation matrix
C_d	Drag coefficient
C_l	Lift coefficient
D	Drag force, [N]
f_i	i^{th} natural frequency, [Hz]
K	Stiffness matrix
L	Lift force, [N]
M	Mass matrix
n_c	Number of measurement channels
O_i	Projection matrix
Q	Covariance matrix of the noise
R	Covariance matrix of the noise
Re	Reynolds number
S	Covariance matrix of the noise
T	Wire tension force, [N]
ux, uy, uz	Uncertainty of the measured displacement by stereo vision in x, y and z directions, [mm]
W	Image window size, [Pixel]
w_k	Process noise in time step of k
$x(t)$	State vector
y_i	Block of measured displacement data at time i
α_i	Angle of attack, [Degree]
Γ	Extended observability matrix
Δ	Extended stochastic observability matrix
ζ_i	i^{th} natural Damping ratio
ν_k	Measurement noise in time step of k
σ	Standard deviation
Φ_i	i^{th} mode shape

List of abbreviation

BL	Base line
CCD	Charge-coupled device
COE	Cost of energy
COV-SSI	Covariance stochastic subspace identification
DD-SSI	Data driven stochastic subspace identification
FOV	Field of view
MAC	Modal assurance criterion
O&M	Operation and maintenance
OMA	Operational modal analysis
SSI	Stochastic subspace identification
SVD	Singular value decomposition
VAWT	Vertical axis wind turbine

accuracy for the technician to install even many sensory markers on a large rotor blade surface. The use of a proper image processing algorithm with two identical cameras, mounted at a fixed distance in between the left and the right camera enables a wide FOV and tracking each marker's displacement in space and time.

Stereo vision has been used in strain and full displacement field analyses with either digital images correlation (DIC), which gives a continuous displacement distribution [6,7], or measuring discrete points on the surface or structure (point tracking approach [12]). However, stereo vision is new in measuring vibration; it shows good correlation with conventional methods like accelerations in this filed [8]. Robustness and simplicity of stereo vision makes it a proper approach for outdoor and large scale experiments. Regarding all these issues, stereo vision shows good potentials for studying the structural and modal properties of wind turbines.

Structural response and modal properties of horizontal axis wind turbines have been studied with stereo vision in recent years. Out of plane blade motions of rotating table fan have been studied using DIC [9], and structural response and modal properties of a full-scale horizontal axis wind turbine have been explored using stereo vision point tracking techniques [10–12]. These works were focused on horizontal axis rotors with blades forming a planar area from the camera perspective. This setup simplifies the problem of detecting deformations which are containing in plane motion (rotor plane), and out of plane motion (normal to the rotor plane and approximately mean wind direction for a horizontal axis wind turbine). In comparison Darrieus rotors operate independently of wind direction changes. Curved or straight bladed segments turn around the main vertical axis and the blades captures a rotor shape space equivalent with a cylinder or a geometrical figure formed as a shape of a catenary. The rotor blade shape with blades under dynamic loading could challenge stereo vison capability in predicting deflections with a representative blade normal pointing in different out of plane directions.

Modal analysis techniques EMA and OMA using stereo vision has demonstrated results agreeing well with results obtained with traditional transducers, and stereo vison calls for easy installation of many markers on a structure and adds capability to present very small modal frequencies [13–15]. Commercial stereo vision systems are expensive for studying modal properties of large structures and also seem to be inherently associated with problems regarding short time histories and uncertainties [15]. It has favoured our strategy for development of a research based stereo vision system.

The paper suggests stereo vision as a less costly way over existing measurement methods for performing deflection and modal analysis of wind turbines, further it explains the non-contact deflection measurements performed on a parked 1 kW VAWT in a wind tunnel. We discuss challenges associated with 1) motion tracking 3-D complex geometries and 2) imperfections in the stereo vision setup, such as the non-ideal baseline distance between the cameras and limited FOV. We aim to prove stereo vision capability in studying small deflection for investigating i) dynamic behaviour of 3-D geometries during vibrations and ii) unsteady aerodynamic effects of a VAWT. This approach is a novel way for exploring the structural dynamics of geometries with components that are not in plane and have complexities such as sharp curvatures and in studying vertical axis rotor dynamics with partly obstructed FOV.

2. Experimental setup

The turbine is a 3-bladed VAWT demonstrator which is mainly designed for DeepWind project and investigated for operation under tilted conditions [16]. The experiment revealed the dynamic behaviour of the Ø2m VAWT rotor, described in Table 1, at 25 m/s during standstill in the open test section of Politechnico Di Milano University[1] wind tunnel.

The demonstrator was placed in the open chamber of the wind tunnel with section dimensions of 4 × 3.84 m^2, as represented in

[1] http://www.windtunnel.polimi.it/english/impianto/impianto.htm.

Table 1
Main characteristics of DeepWind demonstrator.

Rotor height	Max rotor diameter	Blade length	Chord	Blade shape	Airfoil shape
1.870 m	2.030 m	2.781 m	0.101 m	Troposkien	DU-06-W-200

Fig. 1. The wind tunnel is a large scale, closed 2 floor loop facility with a test section in each floor. The current experiment was conducted in the first floor, where a high speed section allows a maximum velocity of 55 m/s at very low turbulence intensity (<1%). During the experiment the wind speed was kept at 25 m/s.

The markers are simple black circles that are attached to the suction and pressure side of the airfoil, and on the rotor shaft surface centrelines (the lines that are passing through the center of masses of all the sections) with a distance of 10 cm between the markers. The marker diameter is 15 mm, which is chosen to occupy 10–20 image pixels in accordance to the distance between camera and the VAWT. There are also a number of markers that are horizontally spaced to investigate the torsional behaviour of the blade.

Two high speed cameras with viewpoints towards the markers were installed at positions close to the test section. The acA2040-180 km Basler cameras were placed about 1.5–2 m apart, and were equipped with 40 mm focal length Nikon lenses. The distance between the cameras and rotor was about 7.5 m. The configuration of the cameras is shown in Fig. 2.

The particular rotor shape of the 3-bladed VAWT, leads to that all the blades and rotor shaft cannot be seen simultaneously by two cameras. In the best situation, 2 blades and rotor shaft would be visible in the stereo image planes. We have upgraded our hardware to provide longer time series at higher sampling frequency, compared to a recent conducted wind turbine stereo vision experiment [15]. With the current hardware, we archived the image acquisition duration of 32 s, with 6000 pictures at a frame rate of 187 frames per second for each camera. The size of each picture is 2048 × 2048 pixel.

Light scene conditions were adjusted for constant light intensity over time and uniform spread over the volume of interest. In order to capture the light in a short exposure time and improve for light imperfections and preventing shadows, several spotlights were installed at different positions.

The cameras were calibrated prior to actual measurement. For this purpose, a wooden plate calibration board 2 m × 2 m with a printed grid of 200 crosses, as seen in Fig. 3, was mounted on the turbine rotor shaft.

The calibration process determines the coordinates of the grid points in image coordinates and in the world coordinate system. With the resulting calibration matrix all image points can be transformed into points of the real world coordinate system [17].

3. Experimental data analysis

3.1. Image processing

Due to the limited FOVs offered by two cameras, only the markers on a fraction of the wind turbine (rotor shaft and the two blades) are visible simultaneously in both cameras. Therefor just the part of the images which includes this fraction is captured, as seen in Fig. 4.

To derive displacement time series from CCD data obtained with the stereo vision camera system, an image processing algorithm was developed. An overview of the image processing algorithm is shown in Fig. 5.

Due to perspective projection, the circular feature is usually deviated into an ellipse in the image plane, depending on the angle and distance between the object and the image plane [18]. This perspective error is corrected based on [18], in the current case and the real center of the circular marker is found.

After targeting the real center of the marker in the left and right camera image frame, and obtaining the line passing through each camera center and real marker center, the space coordinate of the marker center is calculated by using stereo triangulation. Finally, for each point, x-y-z coordinates are obtained for each time step, and an example of applying the above process is seen in Fig. 6.

3.2. Data-driven SSI analysis

The obtained displacement time series were analyzed by using the data driven stochastic subspace identification (DD-SSI) method [19]. The displacement is defined as the position of the point, subtracted from the mean value of the position during the measurement period. The state space model of the multivariate linear system is derived with easy parameterization directly from the measured data. There is no need to solve the highly nonlinear optimizations problem, associated with auto-regressive moving

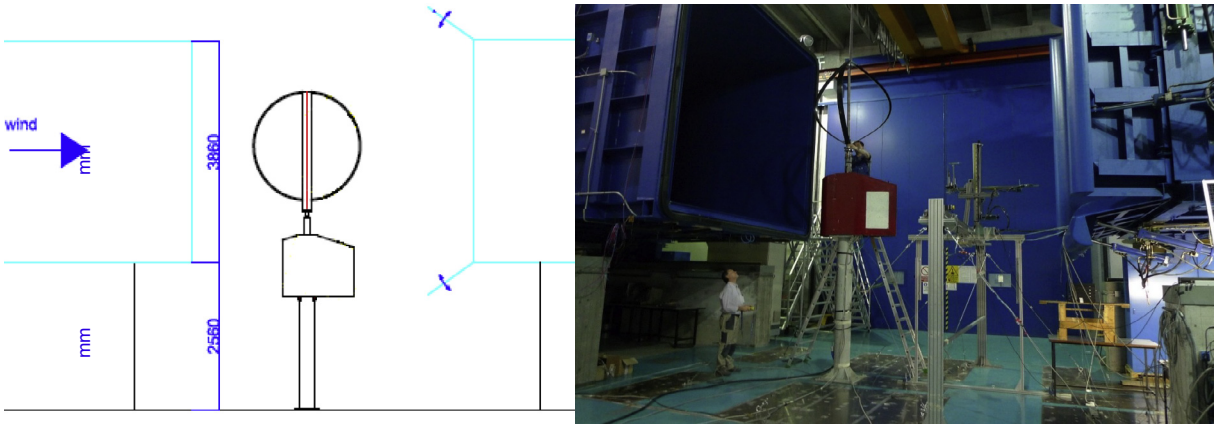

Fig. 1. Turbine position in the wind tunnel of Politecnico Di Milano.

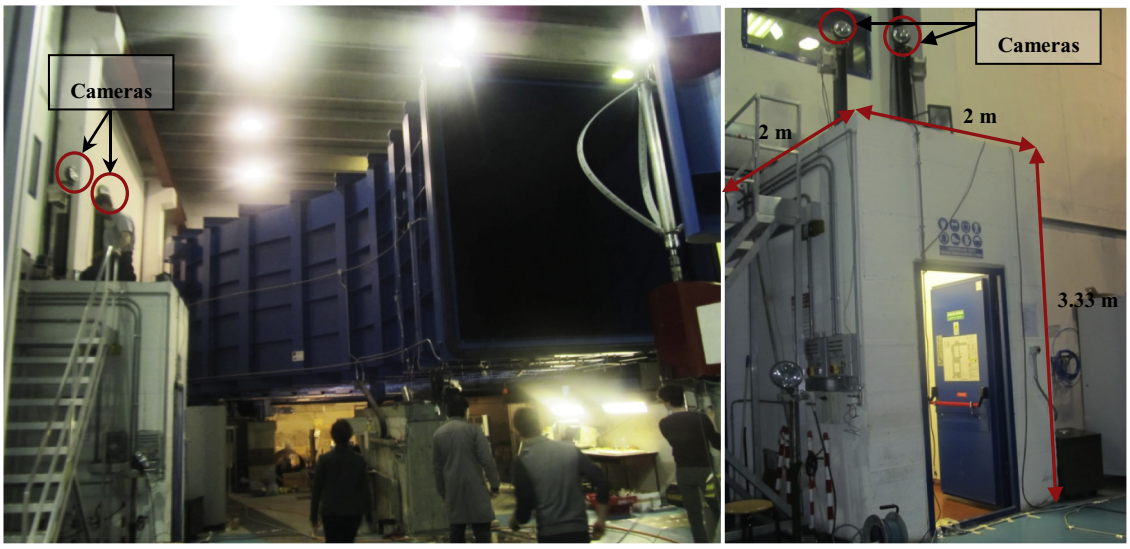

Fig. 2. Camera locations.

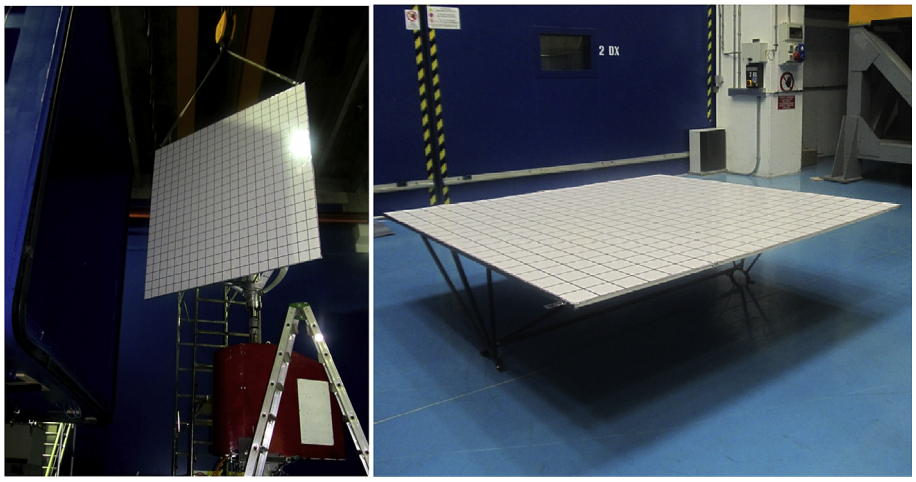

Fig. 3. Right: Calibration board with mounting structure underneath. Left: situation during mounting procedure.

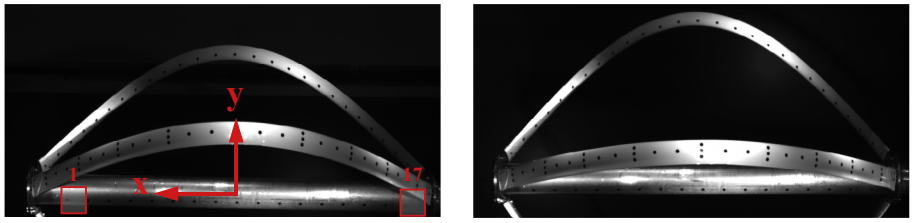

Fig. 4. Left and right images at time$t = 0$. Left image is containing the coordinate system and the image windows number 1 and 17 on the rotor shaft.

average method [20].

The DD-SSI algorithm is based on a stochastic state space model in discrete time as described in Ref. [21]:

$$\begin{aligned} x_{k+1} &= \boldsymbol{A}x_k + w_k \\ y_k &= \boldsymbol{C}x_k + v_k \end{aligned} \tag{1}$$

where $x_k = x(k\Delta t)$ is the discrete time state vector, $\boldsymbol{A} = \exp(A_c\Delta t)$ is the discrete state matrix, Δt is the time step, y_k is the measured output at time $k\Delta t$, and $\boldsymbol{C}$ is the output matrix. w_k is the process noise due to inaccuracies of linear and time invariant state space modelling, and v_k is measurement noise(caused by measurement devices, measurement methods, and assumptions made about distributed and uncorrelated inputs). w_k and v_k are unobserved stationary signals and assumed to follow zero mean and white noise process. On the other hand [19]:

$$E\left[\begin{pmatrix} w_p \\ v_p \end{pmatrix}\begin{pmatrix} w_q^T & v_q^T \end{pmatrix}\right] = \begin{pmatrix} \boldsymbol{Q} & \boldsymbol{S} \\ \boldsymbol{S}^T & \boldsymbol{R} \end{pmatrix}\delta_{pq} \geq 0 \tag{2}$$

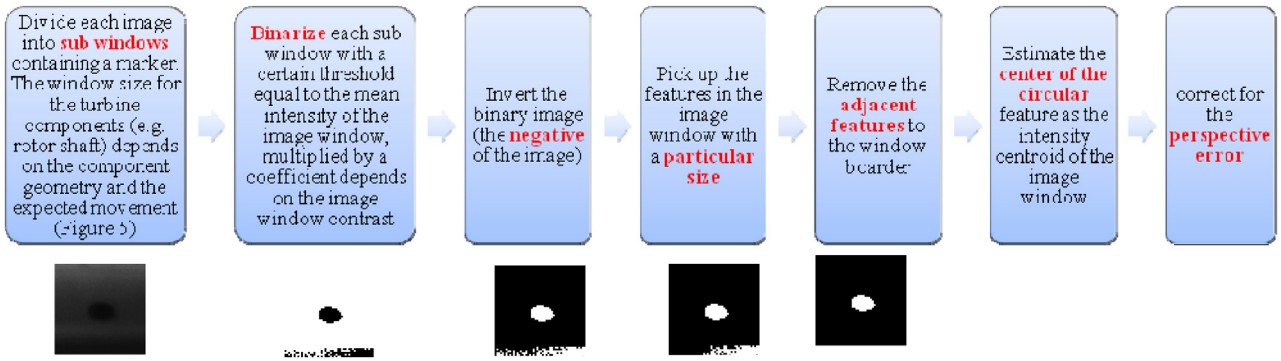

Fig. 5. Image processing algorithm steps.

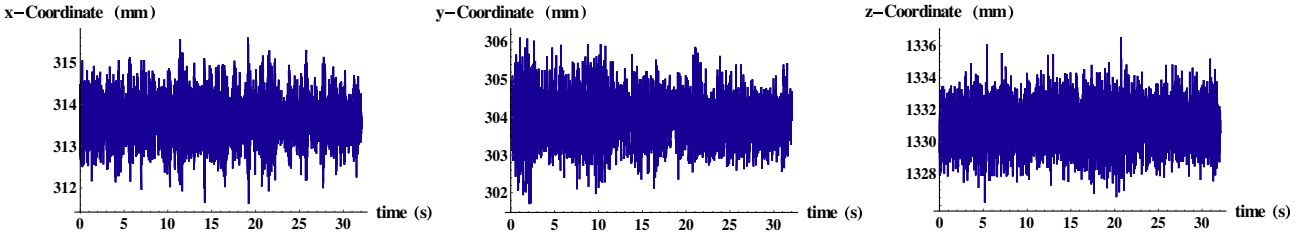

Fig. 6. The position time series for one of blade points in x, y and z direction.

where $\boldsymbol{Q}$, $\boldsymbol{S}$ and $\boldsymbol{R}$ are the covariance matrices of noise signals w_k and v_k, E is the expected value operator and δ_{pq} is the Kronecker delta. Block matrix in equation is assumed to be positive definite [19].

In DD-SSI, data are collected in a block Hankel matrix, where the elements along the diagonal with the constant summation of row and column number are equal [22]. The current block Hankel matrix has $2i$ block rows, N-$2i$+1 columns and n_c rows in each block, so that n_c is the number of measurement channels, N is the number of time steps and i is the model order. More information about the Hankel matrix can be found in Refs. [23] and [24]. Block Hankel matrix can be divided into past and future parts:

$$\boldsymbol{Y}_{0|2i} = \left(\begin{array}{cccc} y_1 & y_2 & \cdots & y_j \\ \cdots & \cdots & \cdots & \cdots \\ y_{i-1} & y_i & \cdots & y_{i+j-2} \\ \hline y_i & y_{i+1} & \cdots & y_{i+j-1} \\ y_{i+1} & y_{i+2} & \cdots & y_{i+j} \\ y_{i+2} & y_{i+3} & \cdots & y_{i+j+1} \\ \cdots & \cdots & \cdots & \cdots \\ y_{2i} & y_{2i-1} & \cdots & y_{2i+j-1} \end{array}\right) = \left(\frac{\boldsymbol{Y}_{0|i}}{\boldsymbol{Y}_{i+1|2i}}\right) = \left(\frac{\boldsymbol{Y}_p}{\boldsymbol{Y}_f}\right) = \frac{\text{“past”}}{\text{“future”}} \tag{3}$$

The projection matrix is a key element in DD-SSI, and described as the projection of the future outputs on the past outputs. The projection matrix is calculated using LQ decomposition of the block Hankel matrix, and the projection matrix is decomposed by the method of singular value decomposition (SVD) [25] into observability matrix (Γ) and Kalman state vector ($\widehat{X}$):

$$\begin{gathered} \boldsymbol{O}_i = (\boldsymbol{U}_1 \quad \boldsymbol{U}_2)\begin{pmatrix} \boldsymbol{S}_1 & 0 \\ 0 & 0 \end{pmatrix}\begin{pmatrix} \boldsymbol{V}_1^T \\ \boldsymbol{V}_2^T \end{pmatrix} = \boldsymbol{U}_1\boldsymbol{S}_1\boldsymbol{V}_1^T = \boldsymbol{\Gamma}_i\widehat{X}_i \Rightarrow \begin{matrix} \boldsymbol{\Gamma}_i = \boldsymbol{U}_1\boldsymbol{S}_1^{1/2} \\ \widehat{X}_i = \boldsymbol{S}_1^{1/2}\boldsymbol{V}_1^T \end{matrix} \\ \boldsymbol{O}_{i-1} = \boldsymbol{\Gamma}_{i-1}\widehat{X}_{i+1} \Rightarrow \widehat{X}_{i+1} = (\boldsymbol{\Gamma}_{i-1})^{+}\boldsymbol{O}_{i-1} \end{gathered} \tag{4}$$

where $\boldsymbol{\Gamma}_{i\text{-}1}$ is obtained by removing n_c rows of the $\boldsymbol{\Gamma}_i$ matrix and $^+$ denotes the Pseudo inverse. There are good researches on capability of SVD in analysing Hankel matrices. [26] and [27] are two good examples of using SVD for the Hankel matrices of noisy time series.

In principle, the number of non-zero singular values in SVD of the projection matrix will be equal to the model order n. In the current cases with the finite length of the time series, all of the singular values are non- zero. According to [28] the dimensions of S_1 are overestimated with physical modes being identified by using an appropriate modal assurance criterion (MAC) number, and a damping ratio criteria. Finally, the state space matrices are estimated [25]:

$$\begin{pmatrix} \widehat{\boldsymbol{A}} \\ \widehat{\boldsymbol{C}} \end{pmatrix} = \begin{pmatrix} \widehat{X}_{i+1} \\ Y_{i|i} \end{pmatrix}\widehat{X}_i \tag{5}$$

The modal assurance criterion (MAC) is a useful tool for checking the repeatability of physical modes. The MAC number is a measure of agreement between two modes and it is calculated between each of the eigenmodes for a certain model order, and for all eigenmodes belonging to the last proceeding model order. If the maximum MAC number is less than the value given by the rejection level, the mode will be regarded as not physical, and it is removed from the stability diagram. More information and mathematical description of MAC can be found in Refs. [28] and [34].

In SSI methods a number of eigenferequencies (eigenvalues) are

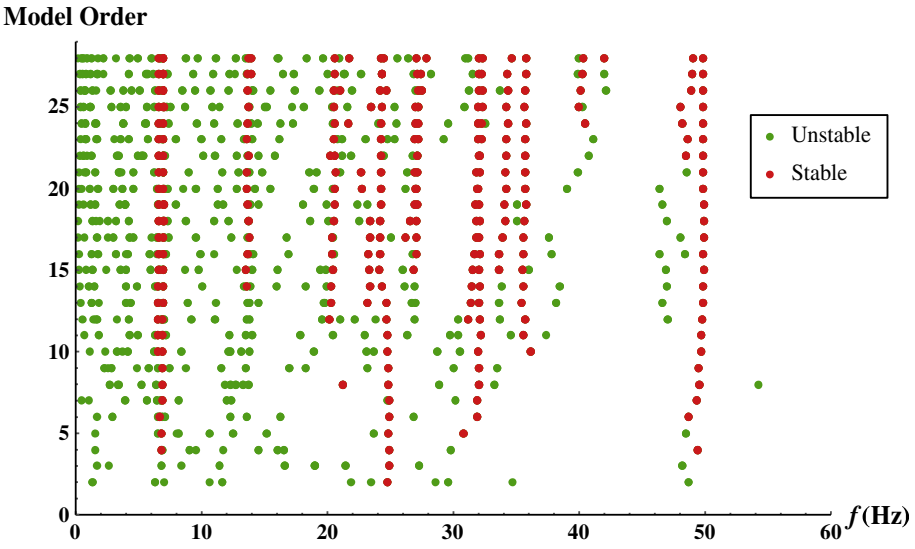

Fig. 7. Stability plot of the parked VAWT rotor response to the wind loading.

calculated for each model order. These eigenvalues are presented in the so called "Stabilization diagram" (stability diagram) that has frequency on X-axis and model order on Y-axis. This plot is an approach to distinguish physical modes. Indeed the physical modes are present in all the model orders, hence they are aligned in the diagram and spurious modes are scattered.

Theoretically, for the ideal case the maximum model order is the rank of the projection matrix where the diagonal elements of the singular value matrix out of SVD drops to a very small value (close to zero). But in the real experiments, there is not such a clear drop in the singular values due to the measurement noises and modelling inaccuracies. Therefore, the model order is usually overspecified to include all the physical modes and the spurious modes are eliminated by knowing that the physical modes have the damping ratio less than a few percent and they are repeated in all the model orders. The MAC criteria is also another tool to distinguish physical modes [29]. For more information about stability diagram refer to [28].

The projection and covariance matrices are closely related, but for the covariance matrix, the error and noise may be squared up by the covariance estimation [30]. For calculating the projection matrix, efficient methods have been established using numerically robust squared root algorithms like QR-factorization [31]. Therefore, theoretically, the numerical behaviour of DD-SSI is better than that of COV-SSI which is based on covariance matrix [32].

3.2.1. DD-SSI results

There were 67 markers applied on the rotor shaft and on the 2 blades (without considering horizontally spaced markers[2]). Each of the markers, measures displacement in 3 directions, therefore $n_c = 67 \times 3 = 201$ for DD-SSI. The number of columns in the Hankel matrix, N-$2i$+1, should be larger than the number of rows $2n_c i$ [19] and the large number of measurement channels decreases the performance of the DD-SSI. Therefore, the measurement points are picked every second to reduce n_c to $35 \times 3 = 105$.

DD-SSI is implemented for model order until 28 and the modal parameters are identified for all the model orders. Covariance matrix of the noise is also calculated in each model order to check the positive definite assumption. The stability diagram is shown in Fig. 7.

The stable poles in the stability plot, which are shown in red, have damping ratios less than 0.04 and MAC number higher than 0.8. The mode shapes corresponding to the stable poles, show that some red lines in the stability diagram (we call them frequency lines hereafter in this text), are not representing structural modes. On the other hand, some of the stable frequencies are related to the effect of the guy wires (which connect the structure under the rotor shaft to the floor) and the flow around the VAWT. The structural modes and the additional effects of the guy wire interactions as well as the frequencies induced by the flow are discussed in the following sections.

Table 2
VAWT natural frequencies obtained with HAWC2 simulation.

Mode No.	1	2	3	4	5	6	7	8
Frequency (Hz)	6.86	6.86	23.09	23.09	23.11	31.60	33.33	50.99

4. Structural modes

4.1. HAWC2 simulation

To understand dynamics of the parked VAWT, the modal contribution of the not observed blade and the frequency lines origin in the stability diagram, a HAWC2 simulation is conducted to predict the structural modes. In Ref. [33] a 2-bladed, floating offshore VAWT is modelled without considering aerodynamics. In the current study, this model is modified into a 3-bladed VAWT model, see Fig. 1. In the model, the entire structure under the rotor is simplified as a long shaft connecting the rotor to the floor, with gross assumptions on mass and stiffness properties, and without a physical model description of the junction between the rotor and the shaft.[3] For more detailed information about the VAWT model refer to [33]. The structural mode shapes are predicted using eigensolver, with no damping included. The natural frequencies and mode shapes are presented in Table 2 and Fig. 8.

[2] SSI analysis is also conducted with horizontally spaced markers to investigate the torsional behaviour; however, no torsional mode was detected. Therefore, they are removed from the next analysis.

[3] Due to time constraints in the Milan wind tunnel, we could not perform a decay test for deriving stiffness and damping data of the support and rotor.

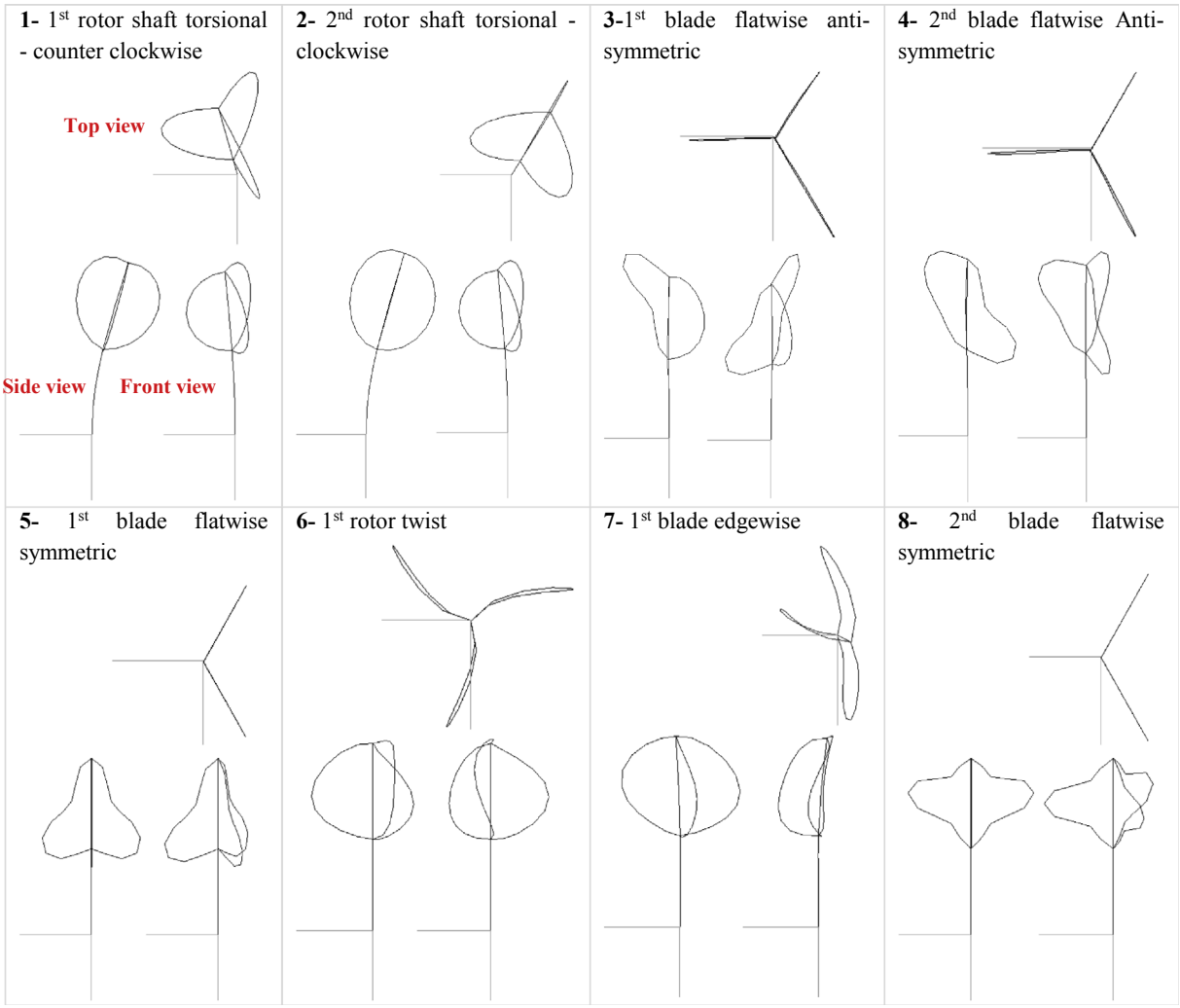

Fig. 8. VAWT mode shapes, obtained with HAWC2 simulation.

The natural frequencies and mode shapes in the wind tunnel experiment are expected to be different from the model, mainly because of neglecting the aerodynamics, and structural properties simplification of the support structure. These differences will be more explained in the next section.

4.2. Wind tunnel experiment

The modal parameters of the structural modes derived from DD-SSI are summarized in Table 3.where σ is the standard deviation and ε is a measure of uncertainty for natural frequency and damping ratio in Table 3 defined as:

Table 3
Natural frequencies and damping ratios of structural modes from DD-SSI.

Mode No.	Frequency (Hz)	σ_f	ε_f	Damping ratio	σ_ζ	ε_ζ
1	6.546	0.037	0.0009	0.012	0.012	0.158
2	6.926	0.032	0.0007	0.010	0.003	0.049
3	24.493	0.300	0.0017	0.012	0.003	0.040
4	27.156	0.172	0.0017	0.018	0.008	0.128
5	31.826	0.304	0.0020	0.014	0.008	0.142
6	32.040	0.281	0.0020	0.009	0.003	0.082
7	49.722	0.271	0.0007	0.015	0.009	0.083

$$\varepsilon_f = \frac{1}{\sqrt{N}} \frac{\sigma_f}{\bar{f}}, \tag{6}$$

where $\bar{f}$ is the mean value of f and N is the number of stable modes. This uncertainty mainly is due to having short displacement time series. The rule of thumb is to record at least $100/n$ seconds (where n is the lowest natural frequency of the structure) [34], which in this case is about 152 s that is much longer than 32 s. There are also other sources of error, such as the uncertainty of the displacement measurement that can be originating from errors in the image processing algorithm, the camera system setup parameters (e.g. BL length), the electronical interferences(data acquisition errors) and environmental factors like temperature. A particular observation from Table 3 is the significant low damping ratio for mode 6 which likely origins from blade edgewise motions coupled with tower torsion and drivetrain vibrations.

The corresponding mode shapes are shown in Fig. 9.

4.3. Comparison of simulated and experimental results

In this section, the in plane mode means the rotor moves in the calibration plane and out of plane mode is when the rotor moves out of the calibration board. Fig. 10 shows the orientation of the

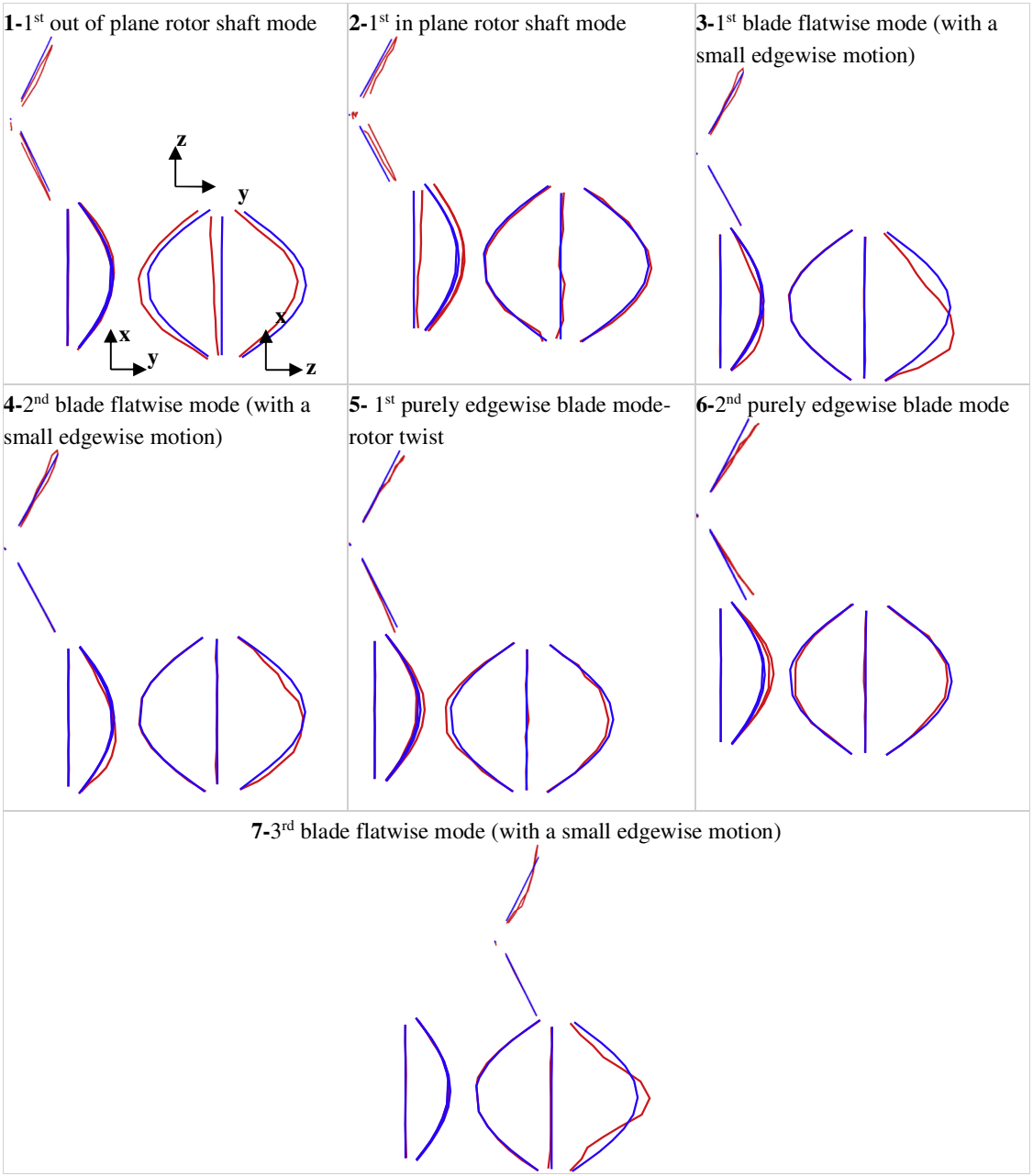

Fig. 9. Structural mode shapes of VAWT rotor from wind tunnel experiment (Blue: initial rotor shape, Red: rotor mode shape), *y* is the main wind direction. (For interpretation of the references to colour in this figure legend, the reader is referred to the web version of this article.)

calibration board in respect to the rotor position within the measurement time. It is seen in Fig. 10 that the calibration board crosses the rotor blades, the reason is that they are representing different times in the same picture: the calibration board is plotted in the calibration time and the rotor is belonging to the measurement time. In the other hand we have done the calibration with a different rotor orientation and then removed the calibration board and changed the orientation of the rotor by rotating the rotor about the rotor shaft to see all the markers on two blades and rotor shaft visible.

In the following table the natural frequencies obtained from simulation and experiment and their percentage difference are presented in Table 4.

The first natural frequency is the first out-of-plane rotor shaft mode, according to Fig. 11. For the next rotor shaft mode, the shaft moves in the main wind direction (y-direction) and therefore it moves in the calibration plane. The rotor shaft natural frequencies, obtained from the experiment, are close to the simulation results. However, the mode shapes are different because of the aerodynamic effects induced by the action of wind, resulting in wind forces acting on the turbine structure in parallel and perpendicular to the wind direction. According to the wind induced forces, the rotor shaft modes are in parallel and perpendicular to the wind direction.

The third and fourth modes are the blade modes. The blade 3 has not been captured in the images, therefore the mode shapes with a similar behaviour of two other blades and a different shape of blade 3, look identical. These two modes contain a larger flatwise and a

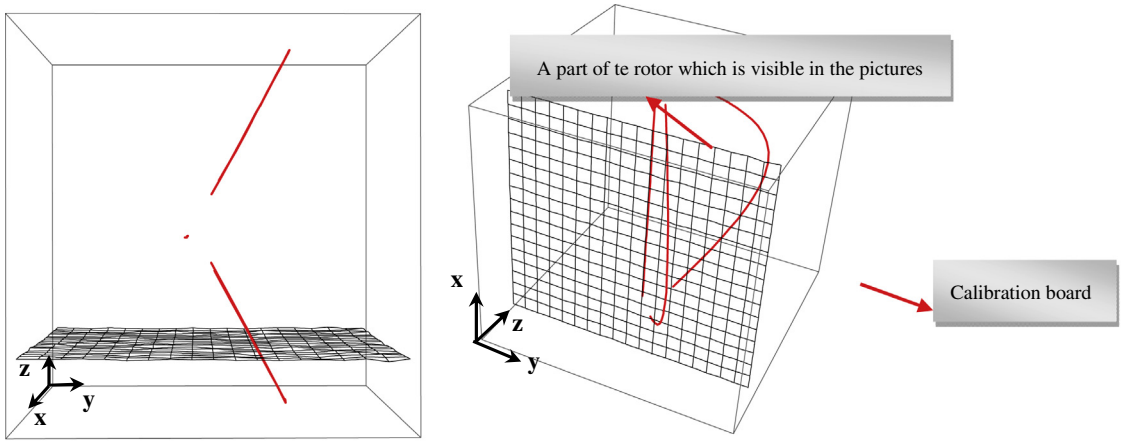

Fig. 10. Orientation of the calibration board in respect to the rotor position within the measurement time.

Table 4
Comparison of the natural frequencies obtained from simulation and experiment.

Mode No.	Frequency (Hz)		Percentage difference
	Simulation	Experiment	
1	6.86	6.546	4.68%
2	6.86	6.926	0.95%
3	23.09	24.493	5.89%
4	23.09	27.156	16.18%
6	23.11	–	–
5	31.60	31.826	0.71%
6	33.33	32.040	3.94%
7	50.99	49.722	2.51%

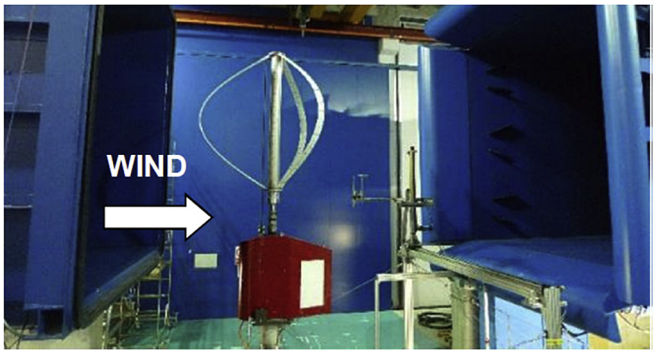

Fig. 11. The blades experience different angle of attacks with respect to the wind direction.

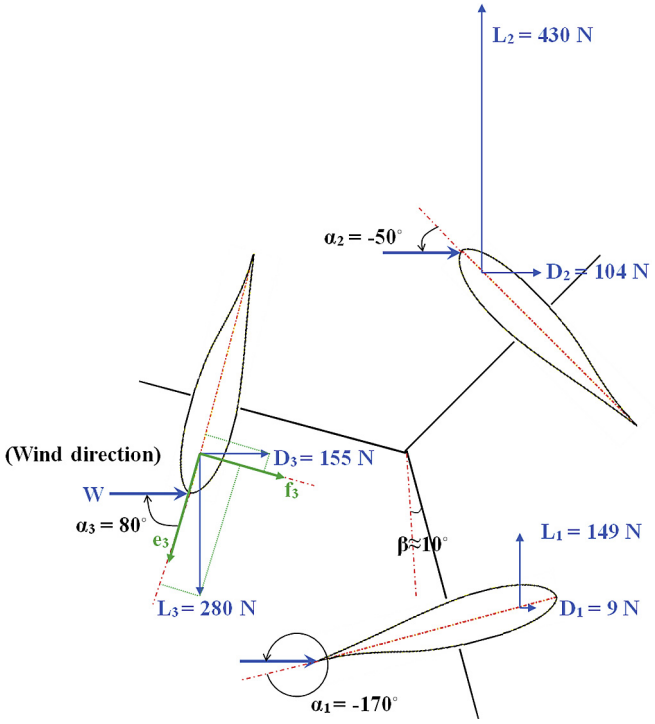

Fig. 12. Blades configuration 1,2,3 during measurements in the wind tunnel.

smaller edgewise motion of one of the blades in the images while the other visible blade in the image does not move. Each of the three turbine blades experiences different angles of attack, therefore the blades must experience different wind loadings and, consequently, different aerodynamic damping; hence, the blades exhibit different modal behaviour. This instability is explained further in the following and also reported on conventional horizontal axis wind turbines [35]. Fig. 11 shows the wind direction regarding to the rotor orientation in wind tunnel.

For the simulated flatwise modes, all three blades contribute with identical loading, material properties and boundary conditions to three flatwise modes. However, during the wind tunnel experiment, one of the blades seemed not to move in flatwise motion. Therefore it seems to exist two flatwise modes. To investigate the difference between the simulated and experimental blade flatwise mode shapes, the aerodynamic loading on each of the blades vs their angles of attack variation is studied. The blade airfoil is DU06-W-200 that is an asymmetric improved version of NACA 0018 airfoil with better aerodynamic performance [36]. The condition of the parked blades configuration, approximate angle of attack, lift (L) and drag (D) forces for blade 1, 2, and 3, are presented in Fig. 12.

According to Fig. 12, flatwise force (f) over edgewise force (e) ratio is much larger for the blade 1 than for the two other blades, i.e. the flatwise force for the blade 1 is four time larger than the edgewise force. The flatwise force is applied on the airfoil suction surface, which is assumed to lead to larger contribution of the aerodynamic damping in the flatwise modes of blade 1. The result indicates that blade 1 is highly damped in flatwise motions due to the aerodynamic loads and it does not move accordingly in flatwise direction.

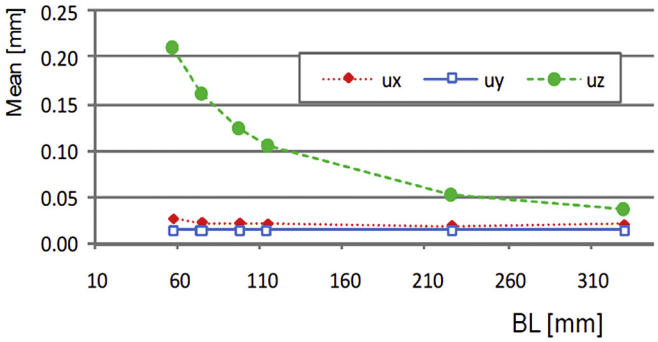

Fig. 13. Mean value of the uncertainty for different baseline (BL) values [40].

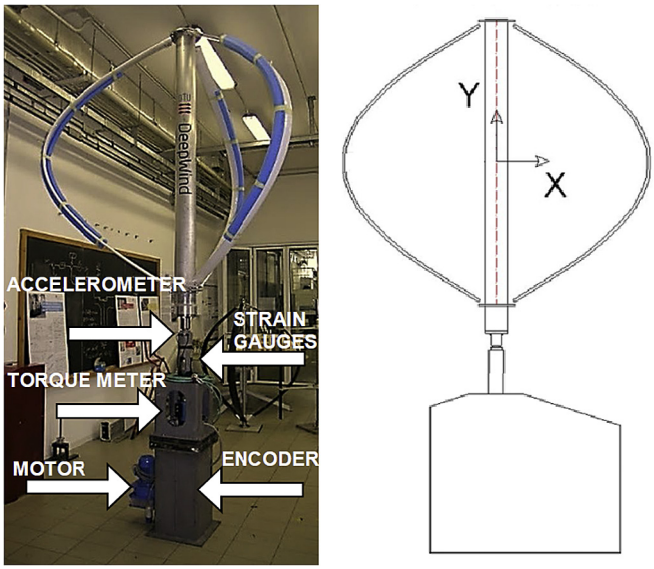

Fig. 14. Left: Sensors configuration on the VAWT, Right: measurement direction.

The difference between the third and the forth modes in Fig. 9, which are mainly flatwise modes, is explained by the presence of the blade 3 having a similar blade shape with blade 2, in the sense of symmetric or anti-symmetric behaviour.

The fifth rotor mode is a rotor twist which is coupled to edge-wise blade mode vibration. In this mode blade 3 is expected to have a similar behaviour as the other blades. The next mode of interest is the second edgewise blade mode. The natural frequencies and mode shapes of these two modes agree well with the simulation results.

In the last identified structural mode, blade 2 seems to exhibit more flatwise and less edgewise motion, which is more likely accompanied with a symmetric or anti-symmetric motion of blade 3. In the simulation results all the blades move in this mode shape, but the experimental results indicate, that the blade 1 does not move in this mode. Indeed, this difference originates from the aerodynamic damping involved in the flatwise modes for the blade 1.

A number of frequency lines in the stability plot (Fig. 7) will not introduce a structural mode shape, as mentioned. The first five modes are harmonics of the first frequency within 3.5% range. By putting a closer look on the turbine fixtures, it is observed that four guy wires fixating the tower to the floor. One of the consequences of the guy wires is the dynamic interference of the structure with the cables [37] while the natural frequencies of the guy wires are harmonics of the first frequency [37]. Therefore it seems, that the mentioned frequencies are interfered by guy wires.

The stability plot in Fig. 7 shows a frequency line at 35.6 Hz that the corresponding mode shape is a cross flow motion of the rotor. To investigate the physical reason of this frequency, the vortex shedding frequency past the rotor is estimated by assuming that the vortex shed past the rotor shaft as a long cylinder with the diameter of 150 mm. Thus according to [38], the frequency induced by the vortex shedding is 33.33 Hz. This number is within 7% of the frequency for the cross flow motion in the stability plot. The vortex shedding past a rotor is more complex than the vortex shedding past a cylinder. Therefore, the assumption of considering the vortex shedding over the rotor as the vortex structure past a cylinder, explains this difference between the calculated vortex shedding frequency and what experiment shows in the stability plot. More detailed information about the guy wire effects and induced vortex shedding frequency in the current case can be found in Ref. [29].

4.4. Uncertainty analysis in stereo reconstruction

The uncertainty of the measured displacement is evaluated by a generalized method based on the law of error propagation in a linear camera model of a stereo vision system. In this method, which is very well described in Ref. [39], the uncertainty in stereo reconstruction propagates in two stages through: calibrations of the cameras and the 3D triangulation to obtain the 3D coordinates from 2D projections in the images.

The baseline length (BL) and the depth of the object with respect to the camera positions are two important factors that affect the uncertainty propagation in the stereo vision process [40], e.g. the uncertainty decreases by having a larger ratio of the BL over the object depth, as it is shown in Fig. 13.

To decrease the uncertainty of the measured displacements, the calibration grid and the circular markers are printed with the high resolution of 1200 *dpi* (dots per inch). In addition the distance between the cameras and the rotor was chosen to be as small as possible. However, there were some limitations in increasing the BL length, such as having limited space to move the cameras and having common FOVs, but it was set to be as large as possible. Since the markers were fully circular, the perspective error due to the 2D projection of the circle into an ellipse was corrected in the image processing algorithm with a corresponding decrease of bias error. Finally, the mean uncertainty for the position determination of all the markers over several time steps was calculated to be (0.145,0.456,1.636) *mm* in *x*, *y* and *z* directions respectively, given that the mean image processing algorithm uncertainty of the image point localization within the motion is 0.06 pixels in both vertically and horizontally directions, and the position of the points in the structures vary as follows in millimetres:

$$760 < x < -950 \;\&\; 414 < y < -136 \;\&\; 1540 < z < -315$$

More details on the uncertainty values for different components of the VAWT are reported in Ref. [29].

Beside all the limitations in increasing the BL over depth ratio the obtained uncertainty is acceptable but it can be improved sufficiently by increasing the BL over depth ratio.

4.5. Spectral analysis of the signals from conventional sensors

The turbine was equipped with two uni-axial accelerometers, 2 strain gauges and a torque meter. Fig. 14 shows an overview of the sensors for the wind turbine.

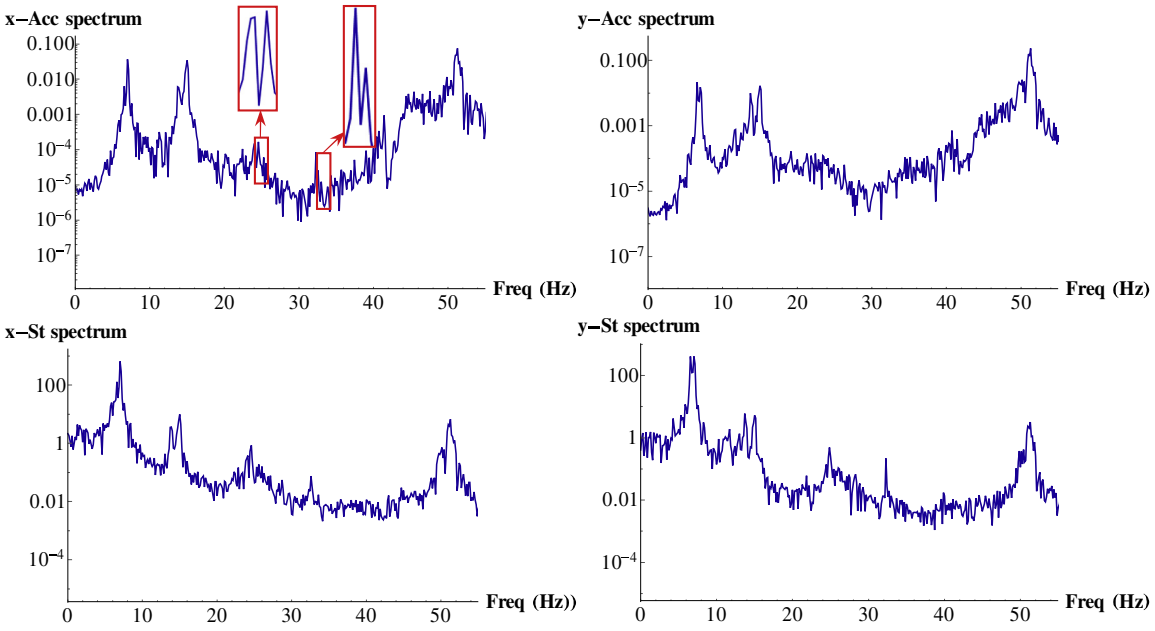

Fig. 15. The logarithmic plot of the spectrum of acceleration (Acc) and strain (St) signals.

The measurement frequency is 2000 Hz for all of the sensors. Fig. 15 shows the spectrum (power spectral density: the Fourier transform of the auto-correlation) of the time series signal that provides basic knowledge of the detected natural frequencies.

In Table 5 the natural frequencies obtained from stereo vision and convectional sensors are compared.

Natural frequencies that are defined by picking the peaks in PDS plots are not as precise as SSI result and it depends on frequency resolution, particularly very closely spaced modes, e.g. the first two blade flatwise modes (modes number 3 and 4 in Table 5), are not well detected in the spectrum. The sensors are mounted under the shaft; therefore the rotor shaft modes are strongly dominant in the spectrum. The first two rotor shaft modes are picked at 6.5 and 7 Hz, and the first blade flatwise modes are picked at 23.9, 24.6. There are two peaks around 32 Hz at 32.3 and 32.6 Hz, where the blade edgewise modes are expected. The peak at 51.6 is also matched to the third blade flatwise mode. Finally the peak at 13.7 is indicating the second guy wire mode. More detailed information about the measurement with conventional sensors during experiment can be found in Ref. [41].

The guy wire interference is observed also in the acceleration and strain signals. There are two other picks in the plots at 15 and 50 Hz that are corresponding to the electrical noise of the sensors regarding to the spectral analysis of the offset signals of the measurement tools with no wind and vibration.

Table 5
Comparison of the natural frequencies obtained from conventional sensors and stereo vision.

Mode No.	Frequency (Hz)		Percentage difference
	Convectional sensors	Stereo vision	
1	6.5	6.546	0.70%
2	7.0	6.926	1.06%
3	23.9	24.493	2.45%
4	24.6	27.156	9.76%
5	32.3	31.826	1.47%
6	32.6	32.040	1.73%
7	51.6	49.722	3.7%

5. Conclusion

The displacements of blades and rotor shaft of a 3-bladed VAWT in the wind tunnel have been measured with a two camera stereo vision in-house built system, and the modal properties of the rotor were estimated by means of OMA using DD-SSI method. The physical modes in the SSI stability plot include the structural and guy wire modes, with explanation on interference from vortex shedding. To support the identification of the rotor structural modes seen in the stability plot, the VAWT rotor was simulated using HAWC2. The simulations were conducted without considering aerodynamics for standstill conditions of the turbine, to predict the structural modes, and the differences between experimental and simulation results are explained by the aerodynamic effects in the wind tunnel. There are also two accelerometers and two strain gauges mounted under the rotor shaft which are measuring during experiment. The spectral analysis of the conventional signals, confirms the frequencies obtained from stereo vision.

This study proves the capability of stereo vision in tracking small deflections of paper markers glued onto stiff blades and rotor shaft surface, making it feasible for studying large structure dynamics, large deflections and aerodynamic effects. In other words, the current study shows the reliability and potential of the stereo vision technique to monitor displacement time series and use it for structural dynamics analysis of large structures. By upgrading the image acquisition system, displacement measurements can be used for modal identification and health monitoring of large structures, such as operating or parked horizontal axis wind turbines. In addition to modal identification, this measurement tool can be very helpful in monitoring the blade tip position to avoid hitting the tower. Finally, the current experiments demonstrated the limitations of using two cameras introducing limited FOV, and this can be solved by adding extra cameras to measure the displacements of VAWTs in operation, or other complicated structures.

References

[1] Paulsen US, et al. DeepWind-from idea to 5 MW concept. Energy Procedia

2014;5:23–33.
[2] Hoffmann K. An introduction to measurements using strain gauges. Darmstadt: Hottinger Baldwin Messtechnik GmbH; 1989.
[3] Fukuda Y, et al. Vision-based displacement sensor for monitoring dynamic response using robust object search algorithm. IEEE Sens. J 2013;13:4725–32.
[4] Park KT, Kim SH, Park HS, Lee KW. The determination of bridge displacement using measured acceleration. J Eng Struct 2005;27:371–8.
[5] Helfrick MN, et al. 3D digital image correlation methods for full-field vibration measurement. J Mech Syst Signal Process 2011;25:917–27.
[6] Helm JD, McNeil SR, Sutton MA. Improved three-dimensional image correlation for surface displacement measurement. J Opt Eng 1996;35:1911–20.
[7] McNeil SR, Peters WH, Sutton MA. Estimation of stress intensity factor by digital image correlation. J Eng Fract Mech 1987;28:101–12.
[8] Waren C, et al. comparison of image based, laser, and accelerometer measurements. In: Proceedings of the IMAC-XXVIII, February 1-4, 2010, Jacksonville, Florida USA; 2010.
[9] Warren C, Niezrecki C, Avitabile P. Optical non-contacting vibration measurement of rotating turbine blades II. In: Proceedings of the IMAC-XXVIII, February 1-4, 2010, Jacksonville, Florida USA; 2010.
[10] Prowell I, et al. Measuring global response of a wind turbine to simulated earthquake shaking assisted by point tracking videogrammetry. In: 52nd AIAA/ASME/ASCE/AHS/ASC structures, structural dynamics and materials conference, 19th 4–7 april 2011, Denver, Colorado; 2011.
[11] Prowell I, et al. Shake table testing of a utility-scale wind turbine. J Eng Mech 2012;138:900–9.
[12] Paulsen US, Erne O, Klein M. Modal analysis on a 500 kW wind turbine with stereo camera technique. In: IOMAC'09 – 3rd international operational modal analysis conference; 2012.
[13] Peeters B, et al. Experimental modal analysis using camera displacement measurements: a feasibility study. In: Sixth international conference on vibration measurements by laser techniques: advances and applications. Proceedings of SPIE, vol. 5503. Bellingham, WA: SPIE; 2004. p. 298–309.
[14] Kohut P, Kurowski P. Application of modal analysis supported by 3D vision-based measurements. J Theor Appl Mech 2009;47:855–70.
[15] Ozbek M, Rixen DJ. Operational modal analysis of a 2.5 MW wind turbine using optical measurement techniques and strain gauges. J Wind Energy 2013;16:367–81.
[16] Battistia L, al. Wind tunnel testing of the DeepWind demonstrator in design and tilted operating conditions. Energy 2016;111:484–97.
[17] Trucco E, Verri A. Introductory techniques for 3-D computer vision. New Jersey, United States: Prentice Hall; 1998.
[18] Heikkila J, Silven O. A four-step camera calibration procedure with implicit image correction. In: Proceedings of IEEE computer society conference on computer vision and pattern recognition, san juan, United States; 1997. p. 1106–12.
[19] Overschee PV, De Moor B. Subspace identification for linear systems. Kluwer Academic Publishers; 1996.
[20] Kirkegaard PH, Andersen P. State space identification of civil engineering structures from output measurements. In: Proceedings of the 15th international modal analysis conference, Orlando, Florida; 1997.
[21] Peeters B, De Reock G. Reference-based stochastic subspace identification for output-only modal analysis. J Mech Syst Signal Process 1999;13:855–78.
[22] Hassani H. Singular spectrum analysis: methodology and comparison. J Data Sci 2007;5:239–57.
[23] Partington JR. An introduction to Hankel operators. Cambridge University Press; 1989.
[24] Peller V. Hankel operators and their applications. New York: Springer; 2003.
[25] Boonyapinyo V, Janesupasaeree T. Data-driven stochastic subspace identification of flutter derivatives of bridge decks. J Wind Energy 2010;98:784–99.
[26] Hassani H, Ghodsi Z. A glance at the applications of Singular Spectrum Analysis in gene expression data. Biomol Detect Quantif 2015;4:17–21.
[27] Hassani H, Zhigljavsky A. Singular spectrum analysis based on the minimum variance estimator. In: Proceedings of the world congress on engineering, London, U.K; 2008.
[28] Rainieri C, Fabbrocino G. Operational modal analysis of civil engineering structures. New York: Springer; 2014.
[29] Najafi N. Experimental vision studies of flow and structural effects on wind turbines. PhD Thesis. Denmark: Technical University of Denmark; 2015.
[30] Golub GH, Van Loan CF. Matrix computations. third ed. The John Hopkins University Press; 1996.
[31] Bincker R, Zhang L, Andersen. Modal identification from ambient response using frequency domain decomposition. In: MAC 18: proceedings of the international modal analysis conference (IMAC), san antonio, Texas, USA; 1999. p. 625–30.
[32] Vaseghi SV. Advanced digital signal processing and noise reduction. John Wiley and Sons, Ltd, Publication; 2008.
[33] Vita L. Offshore vertical Axis wind turbine with floating and rotating foundation. PhD Thesis. Roskilde, Denmark: Risø DTU; 2011.
[34] Brincker R, Ventura C. Introduction to operational modal analysis. United States: Weily; 2015.
[35] Hansen MH. Aeroelastic instability problems for wind turbines. Wind Energy 2007;10:551–7.
[36] Claessens MC. Design and testing of airfoils for application in small vertical Axis wind turbines. Master of Science Thesis. Faculty of Aerospace Engineering: Delft University of Technology; 2006.
[37] Carne TG. Guy cable design and damping for vertical Axis wind turbines. Report. Albuquerque, NM, USA: Sandia National Laboratories; 1980.
[38] White FM. Viscous fluid flow. second ed. McGraw-Hill, Inc; 1991.
[39] Chen J, Ding Z, Yuan F. Theoretical uncertainty evaluation of stereo reconstruction. In: The 2nd international conference on bioinformatics and biomedical engineering, 16–18 may 2008; 2008. pp:2387–2381.
[40] Leo GD, Liguori C, Paolillo A. Propagation of uncertainty through stereo triangulation. In: Instrumentation and measurement technology conference (I2MTC), 2010 IEEE; 2010.
[41] Battisti L, et al. Aerodynamic performance of the 3-blade Deepwind demonstrator report. Italy: Interdisciplinary laboratory of Energetic Technologies Department of Civil, environmental and mechanical engineering University of Trento; 2014.